A simplified structural model of bump-type foil bearings based on contact mechanics including gaps and friction

Mihai Arghir, Omar Benchekroun

A simplified structural model of bump-type foil bearings based on contact mechanics including gaps and friction

Mihai ARGHIR, Omar BENCHEKROUN

PPRIME Institute, UPR CNRS 3346

Université de Poitiers, ENSMA ISAE

86962 Chasseneuil Futuroscope, France

mihai.arghir@univ-poitiers.fr

Abstract

The paper introduces a structural model for bump-type foil bearings based on contact mechanics including gaps and friction. The starting point is a model introduced in [32] were the bump foil is approximated by a specific structure of interacting springs. Following this model, contacts between the top and bump foils and between the bump foil and the sleeve are always closed. Recent analyses [31] showed that this not always verified: contacts can become loose even for very simple loading situations. A new model is then developed for considering these situations. The new model takes into account the elasticity of the top foil and three kind of gaps: between the rotor and the top foil, between the top and the bump foils and between the bump foils and the sleeve. The former model of the bump foil was extended by considering an additional degree of freedom per bump. Friction was modeled with Coulomb law. An efficient numerical procedure borrowed from contact mechanics ([41], [42]) was implemented for solving the structural problem with friction and close/loose gaps. The procedure uses the augmented Lagrangian algorithm for the normal contact forces and the penalty method for the tangential friction force. The procedure is very robust in dealing with stick-slip situations and close/loose contacts. The model was validated by comparisons with results from the literature ([31], [32]).

By considering gaps in the foil structure and close/loose contacts, the model is not only closer to reality but can also handle manufacturing errors of the foil structure. This is shown by considering bump foil height manufacturing errors.

keywords: foil bearing structure; contact mechanics; friction

Introduction

Aerodynamic foil journal bearings represent a technology under scrutiny since decades. They represent a viable, proven technology for small and medium size, high speed rotating machinery operating on air or with gases. The key point of foil bearings is the compliant foil structure that brings a considerable damping compared to the very thin air film during operation. There are many types of foil bearings or, more generally, bearings with a compliant structure. The first bearing of this type, still in use, is the foil leaf bearing. It consists of many beam-like, thin foils that slightly overlap. These kind of bearings have a low ratio of load capacity versus damping. The bump-type foil bearings are more elaborate and use two foils (Figure 1): the smooth top foil and the underneath corrugated foil provided with bumps that act as cross-coupling springs. This kind of foil bearings have better characteristics in terms of load capacity and damping. Another kind of foil bearings use beam-like springs instead of bumps. However, these solutions are less popular.

Among these types, the bump-type foil bearings are the most widely used and analyzed. The difficulties in accurately describing the characteristics of the foil structure are the reason behind systematic research efforts developed for years. An overview of the large number of publications dealing with this subject can be found in the review article [1].

The first model [2], [3] ignored the stiffness of the top foil and considered the bumps as non-interacting springs. By considering the stiffness as being uniformly distributed, the foil structure appeared as a Winkler foundation. Friction was subsidiary taken into account [4] but the model could not predict the damping of the compliant structure and therefore additional viscous damping [5] or structural loss [6] parameters had to be added. This structural model became widespread used due to its easy implementation ([7], [8], [6], [9], [10]). The model was extended by taking into account the top foil.

Carpino et al. [11], [12] introduced a membrane and bending effect of the top foil while the bump foil was still modeled as an elastic foundation. The elastic foundation model was extended in [13] for taking into account radial and circumferential displacements of bumps. Other references modeled the top foil either as a beam or a shell ([14], [15], [16], [17], [18]) in contact with isolated bumps. These latter are described by the stiffness analytic formulas from [4]. The models have the advantage of predicting the sagging effects of the top foil. Moreover, the model in [17] considers also the inertia of the top foil. However, their accuracy can be questioned because they still discard any direct interaction between bumps (a.e. the bending moment that links two successive bumps).

Ku and Heshmat [19] have partially remedied this limitation by adding plate elements between successive bumps and by bookkeeping the different stick-slip state of bumps under load and friction forces. However, this algorithm is quite difficult to implement.

A different category of models discretizes both the top and the bump foil with structural finite elements. Lee et al. [20], [21], [22] modeled the foils with bar and beam elements and took friction into account by using a stick-slip algorithm similar to the one employed in [19]. Lehn et al. [23] used two dimensional shell elements and modeled Coulomb forces with a penalty contact model and a regularized friction law.

A finite element model with a Lagrange multiplier contact model was employed in [24] for foil leaf type bearings but friction was discarded.

Barzem et al. [25] introduced a non-linear model using shell elements for the bumps and for the top foil. The model took into account large (non-linear) deformations of the bumps including buckling. Friction was taken into account following an updated Lagrangian algorithm from Kalker [26].

Larsen et al. [27] adopted a similar approach based on shell elements and large displacements for the bump and the top foil. However, friction was taken into account by using a very specific approach related to penalty method.

Other researchers employed non-linear elasticity commercial codes for modeling the foil structure ([28], [29], [30], [31]). These approaches benefited from the implementation of modern, full non-linear contact and friction algorithms but the models were somewhat difficult to handle due to the large computational effort.

Le Lez and Arghir introduced a different kind of model in 2007 [32]. The model neglected the stiffness of the top foil and modeled the bump foil as a network of interacting trusses behaving like springs. This lead to a linear stiffness matrix of the bump foil defined in a manner similar to the finite element method where each bump is an element. The model was validated by comparison against full non-linear simulations performed with a commercial code [34] and was also coupled to the gas film [35] in journal bearings. Coulomb forces were taken into account by using a dynamic model from [33] where regularized friction forces were estimated from first order differential equations.

Structural models of the bump foil similar to [32] were successfully developed by Hryniewicz et al. [36], Feng and Kaneko [37], Gad and Kaneko [38], von Osmanski [39] or by Hoffman et al. [40]. Some of these models took the top foil into account. The top foil was modeled either as a shell [37], [38] or as a beam [39]. Friction was taken into account using either stick-slip bookkeeping algorithms ([36], [37], [38]) or dynamic, regularized friction forces ([39], [40]). In [39] the inertia of the top and bump foil was also considered in the dynamic model.

The model introduced in [32] is considered as a compromise between accuracy and computational effort because the structural model remains linear while the bumps are fully coupled. However, the model supposes that the contacts between the top and the bump foils as well as the contacts between the bump foil and the sleeve are always closed. This is an ad-hoc assumption aimed to

simplify the numerical algorithm but calculations performed in [31] with a commercial, non-linear elasticity code showed that this not true. Even for very simple loading cases, the contact state might change between loose or close. The model introduced in [32] could not handle these situations because it neglected the top foil stiffness and any possible gaps in the foil structure.

The purpose of the present work is to extend the model introduced in [32] for taking into account close/loose contacts between the top and the bump foil, between the bump foil and the sleeve and between the top foil and the rotor. The top foil stiffness is now taken into account and an additional degree of freedom is added to each bump.

Normal and friction forces between the foils and between the bump foil and the sleeve are solved with the augmented Lagrangian method (Uzawa algorithm) [41], [42]. The contact between the rotor and the top foil is solved with the penalty method.

Comparisons with the models from [32] (linear model) and from [31] (full non-linear) for simple static loadings show hysteresis loops in good agreement. Manufacturing errors of the bump foil are then added to the new model and the results are again compared with [31] showing the same level of agreement. The contact algorithm proved to be very robust and efficient in terms of computational time even for irregular foil structures.

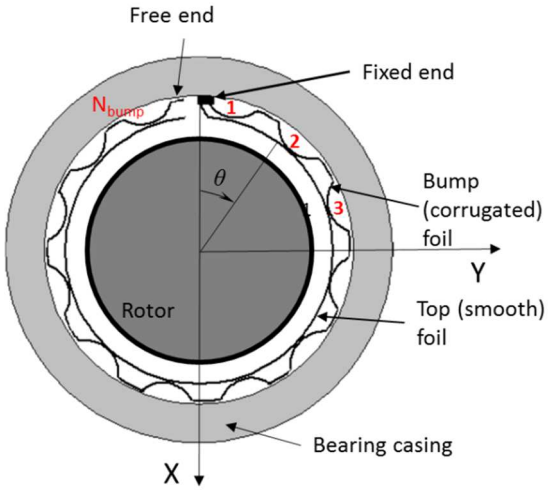

Figure 1. Foil bearing (first generation design)

The foil bearing structure

The gaps

The structural model presented in [32] was based on a linear approximation of the bump foil with structure made of trusses. Curvature effects were neglected and the foil structure was unwrapped. Figure 2 depicts two typical bumps and the associated simplified model. Each bump had three degrees of freedom (DOF), a vertical and a horizontal displacement for the top point of the bump and a horizontal displacement for the point connecting two successive bumps. It was supposed that the

bump foil is continuously in contact with the top foil and with the bearing casing. Moreover, it was supposed that the stiffness of the top foil was negligible compared to the bump foil. Therefore, the structural model neglected the top foil. Closed and open contacts between the bump foil and the top foil and between the bump foil the bearing casing were not taken into account. All contacts were closed and the friction forces were calculated using Coulomb law.

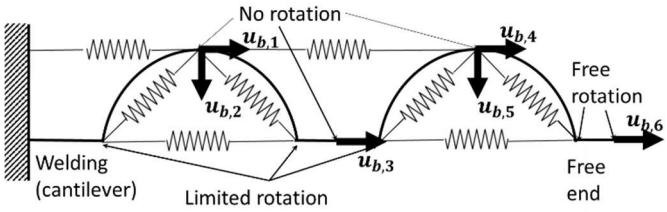

Figure 2. Structural model of the bump foil used in [32] (3DOF per bump)

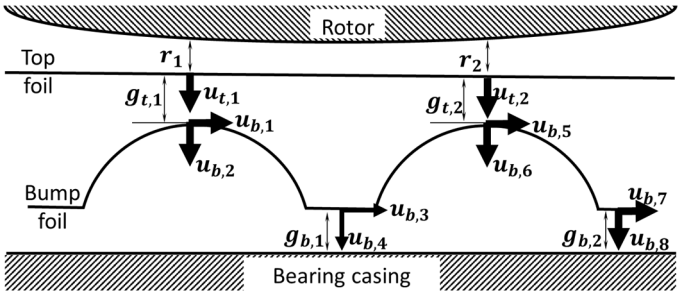

Figure 3. The foil bearing structure with gaps (5DOF per bump)

If the contacts may become loose then additional DOFs must be taken into account as shown in Figure 3. For the contacts between the bump and the top foil, an additional DOF, the radial displacement of the top foil, must be added per bump. The gap between the top foil and the bump foil is:

$$g_{t,i} = g_{0_{t,i}} - u_{t,i} + u_{b,1+2(i-1)} \tag{1}$$

with i the bump number and $g_{0_{t,i}}$ the initial gaps between the bump and the top foil. The non-interference condition between the bump and the top foil is, $g_{t,i} \geq 0$, $i = 1 \dots N_{bump}$.

The gap between the rotor and the top foil can also be described with the aid of the radial displacement of the top foil:

$$g_{r,i} = r_i + u_{t,i} \geq 0 \tag{2}$$

were r_i is the distance between the rotor and the undeformed top foil. [1]

[1] The angle θ is measured from the welding point as shown in Figure 1.

$$r_i = C_r + x_r cos\theta_i + y_r sin\theta_i \tag{3}$$

The non-interference condition is, $g_{r,i} \geq 0, i = 1 \dots N_{bump}$.

An additional DOF must be added to the bump foil if its contacts with the sleeve may become loose. The additional DOF corresponds to the radial displacement of the bottom node of the bump (Figure 3). The gap between the bump foil and the sleeve is:

$$g_{b,i} = g_{0_{b,i}} - u_{b,2+2(i-1)} \tag{4}$$

where $g_{0_{b,i}}$ are the initial gaps between the bump foil and the sleeve. The non-interference condition between the bump and sleeve is, $g_{b,i} \geq 0, i = 1 \dots N_{bump}$.

Due to the additional DOFs a stiffness matrix for the top foil must be introduced and the stiffness matrix of the corrugated bump foil must be reviewed.

The stiffness of the top foil

The top foil is modeled as a circular (curved) beam with the appropriate plate correction. The beam end corresponding to the welding is fixed while the other end is free (Figure 1). The discretization nodes correspond to the top of the bumps and each node has a one DOF represented on the unwrapped foil on Figure 3 as a vertical displacement, $u_{t,i}$ (downwards positive). For the circular beam $u_{t,i}$ corresponds to a radial displacement (outwards positive). The elasticity matrix is obtained with the aid of Bresse formulas and yields:

$$s_{i,j} = \frac{R^3}{Le^3/12}\frac{1-\nu^2}{E}\begin{cases} \dfrac{cos\theta_i sin\theta_j}{2} - \dfrac{\theta_j cos(\theta_i - \theta_j)}{2}, if\ \theta_j \leq \theta_i \\ \dfrac{cos\theta_j sin\theta_i}{2} - \dfrac{\theta_i cos(\theta_j - \theta_i)}{2}, otherwise \end{cases} \tag{5}$$
$$\theta_i, \theta_j > 0, i, j = 1 \dots N_{bump}$$

The stiffness matrix of the top foil is then:

$$\boldsymbol{K_t} = \boldsymbol{S}^{-1} \tag{6}$$

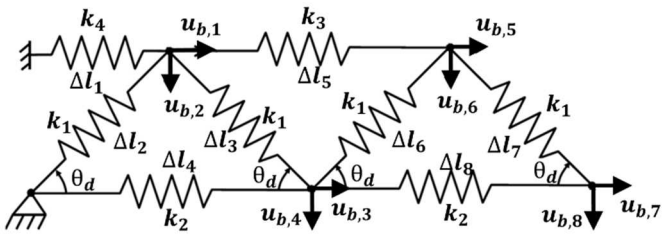

Figure 4. Discretization of the bump foil with 4DOF per bump

The stiffness of the bump foil

The stiffness of the bump foil with 3 DOF per bump was presented in [32]. For the bump foil with 4DOF per bump, the parameters $k_1 \ldots k_4$ and θ_d depicted in Figure 4 remain the same as in [32] but an additional DOF, namely the vertical displacement of the bump bottom, $u_{b,2+2(i-1)}$ must be taken into account. For example, the potential energy of the corrugated foil with two bumps depicted in Figure 4 is:

$$\Pi_{2b} = \frac{1}{2}\left[k_1\left(\Delta l_2{}^2 + \Delta l_3{}^2 + \Delta l_6{}^2 + \Delta l_7{}^2\right) + k_2\left(\Delta l_4{}^2 + \Delta l_8{}^2\right) + k_3 \Delta l_5{}^2 + k_4 \Delta l_1{}^2\right] \quad (7)$$

$$\begin{aligned} \Delta l_1 &= u_1 & \Delta l_5 &= u_3 - u_1 \\ \Delta l_2 &= u_1 c - v_1 s & \Delta l_6 &= u_3 c - v_3 s - u_2 c + v_2 s \\ \Delta l_3 &= u_2 c - u_1 c - v_1 s + v_2 s & \Delta l_7 &= u_4 c - u_3 c - v_3 s + v_4 s \\ \Delta l_4 &= u_2 & \Delta l_8 &= u_4 - u_2 \end{aligned}$$

where $c = cos\theta_d$, $s = sin\theta_d$ and its DOF are the elements of the following vector:

$$\boldsymbol{u_{2b}} = \{u_{b,1} \quad u_{b,2} \quad u_{b,3} \quad u_{b,4} \quad u_{b,5} \quad u_{b,6} \quad u_{b,7} \quad u_{b,8}\}^T \quad (8)$$

The stiffness matrix is obtained by deriving the potential energy Π_{2b} following each DOF. This yields:

(9)

$$\boldsymbol{K_{2b}} = \begin{bmatrix} 2k_1c^2 + k_3 + k_4 & 0 & -k_1c^2 & -k_1cs & -k_3 & 0 & 0 & 0 \\ 0 & 2k_1s^2 & -k_1sc & -k_1s^2 & 0 & 0 & 0 & 0 \\ -k_1c^2 & -k_1cs & 2k_2 + 2k_1c^2 & 0 & -k_1c^2 & k_1cs & -k_2 & 0 \\ -k_1sc & -k_1s^2 & 0 & 2k_1s^2 & k_1sc & -k_1s^2 & 0 & 0 \\ -k_3 & 0 & -k_1c^2 & k_1cs & k_3 + 2k_1c^2 & 0 & -k_1c^2 & -k_1cs \\ 0 & 0 & k_1cs & -k_1s^2 & 0 & 2k_1s^2 & -k_1sc & -k_1s^2 \\ 0 & 0 & -k_2 & 0 & -k_1c^2 & -k_1sc & k_2 + k_1c^2 & k_1cs \\ 0 & 0 & 0 & 0 & -k_1sc & -k_1s^2 & k_1sc & k_1s^2 \end{bmatrix}$$

This matrix can be cast as the sum of individual stiffness matrixes of each bump plus a coupling matrix (Appendix 1).

The contact model

The mathematical model of the aerodynamic foil bearing structure must include the rotor, the top, the bump foil and the bearing casing plus the non-interference constraints that link these four elements. The non-interference constraints are expressed with the aid of the gap functions described by (1)-(4). If the gap functions are positive, then contacts are loose and the normal and the tangential contact forces are zero. On the other hand, if the gap functions are nil, then the contacts are closed and the normal forces are non-zero. This is mathematically expressed by the following equations:

$$g_i \geq 0, F_{n,i} \leq 0, g_i F_{n,i} = 0 \quad (10)$$

where g_i stands for any of the gap functions and $F_{n,i}$ for the corresponding normal contact forces. In contact mechanics, these are known as the Hertz-Signorini-Moreau conditions [41].

The elastic problem of the foil structure is solved by minimizing the potential energy of the elastic structure (i.e. a functional) Π,

$$\Pi = \frac{1}{2}\boldsymbol{u_b}^T \boldsymbol{K_b} \boldsymbol{u_b} + \frac{1}{2}\boldsymbol{u_t}^T \boldsymbol{K_t} \boldsymbol{u_t} \tag{11}$$

with constraints issued from contact conditions, $g_i \geq 0$.

The methods usually adopted in contact mechanics include the effect of constraints into the potential energy of the elastic structure. The penalty method, the Lagrange multiplier method or the augmented Lagrange method can be employed. Each method has its advantages and drawbacks. For the penalty method the extended functional of the potential energy is:

$$\Pi_P = \Pi + \frac{1}{2}\varepsilon_P \boldsymbol{g}^T \boldsymbol{g} \tag{12}$$

where g in eq. (12) are the constraints for the contacts supposed to be closed (contacts supposed loose are not included) and ε_P is a parameter similar to a spring stiffness. For high accuracy ε must be of the order 10^{12} N/m or larger. The method has the advantage of being simple because the stiffness matrix obtained when minimizing Π_P has the same size as the linear elastic stiffness matrix. However, it includes the parameters ε that might damage its conditioning.

For the Lagrange multipliers method the extended functional of the potential energy is:

$$\Pi_{LM} = \Pi + \boldsymbol{\lambda}^T \boldsymbol{g} \tag{13}$$

where the Lagrange multiplier λ is part of the solution and represents the normal contact force. As in the previous method, the Lagrange multipliers are added only for the contacts supposed to be closed. The stiffness matrix obtained by minimizing Π_{LM} is well conditioned but its size is not a priori known (it must include the Lagrange multipliers and therefore depends on the number of contacts supposed to be closed). Compared to the linear stiffness matrix of the elastic structure without constraints, the extended matrix it is not positive definite any more.

The augmented Lagrange method avoids the ill conditioning problems of the penalty method and the problems related to the variable size of then extended matrix of the Lagrange multipliers method. The extended functional of the potential energy is :

$$\Pi_{ALM} = \Pi + \bar{\boldsymbol{\lambda}}^T \boldsymbol{g} + \frac{1}{2}\varepsilon_{ALM} \boldsymbol{g}^T \boldsymbol{g} \tag{14}$$

and the Lagrange multipliers $\overline{\lambda}$ are iteratively updated following Uzawa algorithm [42]:

$$\overline{\boldsymbol{\lambda}}_{new} = \overline{\boldsymbol{\lambda}}_{old} + \varepsilon_{ALM}\boldsymbol{g}_{new} \tag{15}$$

The iterative algorithm can start with $\overline{\lambda}_0 = 0$ and with a limited value of the parameter ε_{ALM} for preserving the conditioning of the resulting stiffness matrix. The bar notation $\overline{\lambda}$ denotes that the Lagrange multipliers are kept constant and are updated only within what is addressed as "outer" iterations loop. Their significance is the same, i.e. normal contact forces.

If friction forces are discarded, the advantages and drawbacks of these three methods were mentioned above. However, when friction forces are present the advantage of the augmented Lagrange method becomes clear.

The Coulomb friction force

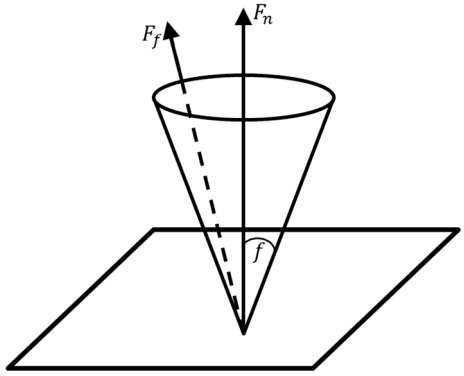

Figure 5. The friction cone of the Coulomb law

The friction forces are described by the Coulomb law. In its natural form this law is written in terms of the sliding velocity, $\dot{u}_{tg}$.

$$\left\|F_f\right\| \leq f|F_n| \text{ so that } \begin{cases} if\ \left\|F_f\right\| < f|F_n|\ then\ \dot{u}_{tg} = 0, (stick) \\ otherwise\ \left\|F_f\right\| = f|F_n|\ and\ \exists\gamma > 0\ so\ that\ \dot{u}_{tg} = -\gamma F_f, (slip) \end{cases} \tag{16}$$

The friction cone graphically depicts Coulomb law (Figure 5). The law is not conservative; therefore, the potential energy of the contact problem with friction has no minimum anymore. The functional (i.e. the potential energy) associated to Signorini's problem with Coulomb friction is nonconvex, nonquadratic and nondifferentiable. Thus, standard uniqueness and existence results from convex analysis cannot be applied. However, the solution has been shown to exist for sufficiently small friction coefficients [41].

A fixed point iteration method in the normal force is used for the numerical solution of this problem. A contact problem with the so called Tresca friction will be solved at every iteration step. The Tresca friction law is a reduced frictional problem with a prescribed normal force. It is expressed in the same way as the Coulomb law

$$\|F_f\| \leq G \text{ so that } \begin{cases} if\ \|F_f\| < G\ then\ \dot{u}_{tg} = 0, (stick) \\ otherwise\ \|F_f\| = G\ and\ \exists \gamma > 0\ so\ that\ \dot{u}_{tg} = -\gamma G, (slip) \end{cases} \quad (17)$$

where $G = f|\bar{F}_n|$ and $\bar{F}_n$ is the prescribed normal force. The bar in the notation of the normal force indicates it remains constant during the iterative algorithm for the calculation of the friction force F_f. This will be addressed as the "inner" iterations loop. The bar notation also indicates the link between the prescribed nodal force and the Lagrange multipliers in the augmented Lagrange algorithm. In fact $\bar{F}_n$ will be exactly the Lagrange multipliers $\overline{\lambda}$ updated in an « outer » iterations loop.[2]

In the "inner" iterations loop, the friction forces are calculated depending on the stick or slip state. It is supposed that closed contacts are initially in stick state and the friction force is described by a penalty approach.

$$F_f^{trial} = \varepsilon_f \left(u_{tg}^{(k)} - u_{tg}^{(0)} \right) \quad (18)$$

where $u_{tg}^{(k)}$ is the tangential displacement[3] at iteration *(k)* and $u_{tg}^{(0)}$ is the tangential displacement at the previous time or loading step. The corresponding potential energy is:

$$\frac{1}{2} \varepsilon_f \left(u_{tg}^{(k)} - u_{tg}^{(0)} \right)^2 \quad (19)$$

and is added to the total potential energy of the structure. The displacements of the structure are calculated by minimizing the total potential energy in a step that will be further detailed. After updating the displacements of the structure, $u^{(k)}$, the trial value of the friction force (18) can be estimated and the algorithm checks for stick or slip state:

$$\begin{cases} if\ \left|F_f^{trial}\right| < f|\bar{F}_n|\ then\ F_f^{(k)} = F_f^{trial}\ (stick\ state) \\ otherwise\ F_f^{(k)} = f\bar{F}_n sign\left(\dot{u}_{tg}^{(k)}\right)\ (slip\ state) \end{cases} \quad (20)$$

[2] The Tresca approximation of the friction force described by eq. (18) can be interpreted as a solution search inside of a cylinder instead of a cone.

[3] For the present problem, these are lateral displacements of the bump top and bottom points. For a general case, these are relative displacements between the two sliding surfaces.

where it should be reminded that following the Hertz-Signorini-Moreau conditions, $\bar{F}_n < 0$. It is to be underlined that for the stick state, $u_{tg}^{(k)}$ and $u_{tg}^{(0)}$ are very close but not exactly equal. Following the penalty approach, the largest the value of the "stiffness" ε_f, the lowest the error $\left\| u_{tg}^{(k)} - u_{tg}^{(0)} \right\|$.

In the next iteration, nodes that are in a stick state are continued to be dealt with the penalty method and their contribution to the total potential energy is given by eq. (19) but the contribution of nodes that are in slip state is described by the mechanical work of the friction force:

$$F_f^{(k)} \left(u_{tg}^{(k)} - u_{tg}^{(0)} \right) = f \bar{F}_n sign\left(\dot{u}_{tg}^{(k)} \right) \left(u_{tg}^{(k)} - u_{tg}^{(0)} \right) \tag{21}$$

The displacements of the structure are calculated again by minimizing the total potential energy that includes the mechanical work of friction forces in slip state (21).

The state of the friction force may change again between stick and slip. Therefore, the "inner" iteration loop is repeated until there is no change of the state of the friction forces. The convergence is possible because the normal contact forces (i.e. the Lagrange multipliers) are kept constant during the "inner" iteration loop. The advantage of the augmented Lagrange method is now clear.

The total potential energy and the "inner" iterations loop

Following the described algorithm, the total potential energy of the bump foil structure is:

$$\begin{aligned} \Pi_{ALM}(x) = & \frac{1}{2} \boldsymbol{u_b}^T \boldsymbol{K_b} \boldsymbol{u_b} + \frac{1}{2} \boldsymbol{u_t}^T \boldsymbol{K_t} \boldsymbol{u_t} \\ & + \sum_{i=1}^{N_{cntct}} \left(\bar{\lambda}_i g_i + \frac{1}{2} \varepsilon_{ALM} g_i^2 \right) \\ & + \frac{1}{2} \sum_{i=1}^{N_{stick}} \varepsilon_f \left(u_{b,i} - u_{b,i}^{(0)} \right)^2 - \sum_{i=1}^{N_{slip}} \underbrace{f \bar{\lambda}_i sign\left(\dot{u}_{b,i} \right)}_{F_{f,i}} \left(u_{b,i} - u_{b,i}^{(0)} \right) \\ & + \frac{1}{2} \sum_{i=1}^{N_{Rotor}} \varepsilon_r g_{r,i}^2 \end{aligned} \tag{22}$$

where N_{cntct} are all nodes where the contacts between bumps/top foil and bumps/sleeve are assumed to be closed ($N_{cntct} \leq 2N_{bump}$), N_{stick} and N_{slip} are the nodes with friction state stick and slip, respectively[4] and N_{Rotor} are the nodes where the rotor interferes with the top foil $N_{Rotor} \leq N_{bump}$. The third term on the right hand side of eq. (22) corresponds to the potential energy due to bump normal contacts (thus the gap functions g_i are either $g_{t,i}$ or $g_{b,i}$), the fourth term is the potential energy due to nodes that are in stick state, the fifth term corresponds to the mechanical work of slip friction forces and the sixth term is the potential energy due to the interference between

[4] $N_{cntct} = N_{stick} + N_{slip}$, $N_{stick} \cap N_{slip} = \emptyset$

the rotor and the top foil. The penalty parameters acting like springs $\varepsilon_{ALM}, \varepsilon_f, \varepsilon_r$ have different values and generally, $\varepsilon_{ALM} \ll \varepsilon_f, \varepsilon_r$.

For example, the equations of the algorithm can be detailed for a foil structure with one bump following the notations used in Figure 3. The extension to an arbitrary number of bumps is immediate.

$$\begin{aligned}\Pi_{ALM} = &\frac{1}{2}\boldsymbol{u_b}^T\boldsymbol{K_b}\boldsymbol{u_b} + \frac{1}{2}K_t u_t^2 \\ &+\bar{\lambda}_t\left(g_{0_t} - u_t + u_{b,2}\right) + \frac{1}{2}\varepsilon_{ALM}\left(g_{0_t} - u_t + u_{b,2}\right)^2 \\ &+\bar{\lambda}_b\left(g_{0_b} - u_{b,4}\right) + \frac{1}{2}\varepsilon_{ALM}\left(g_{0_b} - u_{b,4}\right)^2 \\ &+\frac{1}{2}\varepsilon_f\left(u_{b,1} - u_{b,1}^{(0)}\right)^2 ISTICK_t - \underbrace{f\bar{\lambda}_t sign\left(\dot{u}_{b,1}\right)}_{F_{f,t}}\left(u_{b,1} - u_{b,1}^{(0)}\right)(ISTICK_t - 1) \\ &+\frac{1}{2}\varepsilon_f\left(u_{b,3} - u_{b,3}^{(0)}\right)^2 ISTICK_b - \underbrace{f\bar{\lambda}_b sign\left(\dot{u}_{b,3}\right)}_{F_{f,b}}\left(u_{b,3} - u_{b,3}^{(0)}\right)(ISTICK_b - 1) \\ &+\frac{1}{2}\varepsilon_r(r + u_t)^2\end{aligned} \tag{23}$$

where *ISTICK=1* when the contact is stick and *ISTICK=0* otherwise (i.e. slip).

The minimization of the total potential energy following the degrees of freedom of the problem yields:

$$\begin{aligned}\frac{\partial\Pi_{ALM}}{\partial u_{b,1}} &= \sum_{j=1}^{4} K_{b_{1,j}}u_{b,j} + \varepsilon_f\left(u_{b,1} - u_{b,1}^{(0)}\right)ISTICK_t - f\bar{\lambda}_t sign\left(\dot{u}_{b,1}\right)(ISTICK_t - 1) = 0 \\ \frac{\partial\Pi_{ALM}}{\partial u_{b,2}} &= \sum_{j=1}^{4} K_{b_{2,j}}u_{b,j} + \bar{\lambda}_t + \varepsilon_{ALM}\left(g_{0_t} - u_t + u_{b,2}\right) = 0 \\ \frac{\partial\Pi_{ALM}}{\partial u_{b,3}} &= \sum_{j=1}^{4} K_{b_{3,j}}u_{b,j} + \varepsilon_f\left(u_{b,3} - u_{b,3}^{(0)}\right)ISTICK_b - f\bar{\lambda}_b sign\left(\dot{u}_{b,3}\right)(ISTICK_b - 1) = 0 \\ \frac{\partial\Pi_{ALM}}{\partial u_{b,4}} &= \sum_{j=1}^{4} K_{b_{4,j}}u_{b,j} - \bar{\lambda}_b - \varepsilon_{ALM}\left(g_{0_b} - u_{b,4}\right) = 0 \\ \frac{\partial\Pi_{ALM}}{\partial u_t} &= K_t u_t - \bar{\lambda}_t - \varepsilon_{ALM}\left(g_{0_t} - u_t + u_{b,2}\right) + \varepsilon_r(r + u_t) = 0\end{aligned} \tag{24}$$

In a matrix form:

$$\underbrace{\left(\begin{bmatrix} \boldsymbol{K_b} & 0 \\ 0 & K_t \end{bmatrix} + \begin{bmatrix} \varepsilon_f ISTICK_t & 0 & 0 & 0 & 0 \\ 0 & \varepsilon_{ALM} & 0 & 0 & -\varepsilon_{ALM} \\ 0 & 0 & \varepsilon_f ISTICK_b & 0 & 0 \\ 0 & 0 & 0 & \varepsilon_{ALM} & 0 \\ 0 & -\varepsilon_{ALM} & 0 & 0 & \varepsilon_{ALM} + \varepsilon_r \end{bmatrix}\right)}_{[K_{ALM}]} \begin{Bmatrix} u_{b,1} \\ u_{b,2} \\ u_{b,3} \\ u_{b,4} \\ u_t \end{Bmatrix} \quad (25)$$

$$= \begin{Bmatrix} \varepsilon_f u_{b,1}^{(0)} ISTICK_t + f\bar{\lambda}_t sign(\dot{u}_{b,1})(ISTICK_t - 1) \\ -\bar{\lambda}_t - \varepsilon_{ALM} g_{0_t} \\ \varepsilon_f u_{b,3}^{(0)} ISTICK_b + f\bar{\lambda}_b sign(\dot{u}_{b,3})(ISTICK_b - 1) \\ \bar{\lambda}_b + \varepsilon_{ALM} g_{0_b} \\ \bar{\lambda}_t + \varepsilon_{ALM} g_{0_t} - \varepsilon_r r \end{Bmatrix}$$

The sign function is discontinuous and thus strongly non-linear. Therefore, it is replaced by a continuous approximation and a Newton-Raphson algorithm explained in Appendix 2 can now solve the non-linear system.

The "outer" iterations loop

After solving for friction forces, the Lagrange multipliers are updated following eq. (15) in an "outer" iterations loop. It was previously stated that the Tresca approximation of the friction force described by eq. (17) can be interpreted as a solution search inside of a cylinder. Figure 6 then shows how Tresca friction cylinders approximate the Coulomb friction cone. A structured pseudo-code of the "inner" and "outer" iterations loops for friction and normal forces, respectively, is given in Figure 7. The "inner" and "outer" lops can be also identified on the flowchart depicted in Figure 17 of the Appendix 3.

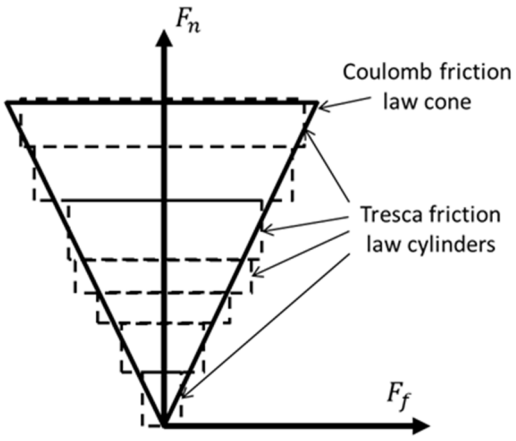

Figure 6. The approximation of the Coulomb friction cone by Tresca friction cylinders

```
! Start Uzawa algorithm
λ=0
LOOP while (error_lagrange>precision_lagrange) ! begin calculation of the normal forces
    iter_frctn=0
    err_frctn=BIG
    LOOP while (err_frctn≠0) ! begin calculation of the friction forces
        IF(iter_frctn=0) THEN ! All contacts are in stick state
        CALCULATE the extended stiffness matrix and the RHS term considering stick/slip state of the contacts
        CALCULATE displacements from the NEWTON solution of the non-linear system [K]{u_b v_β}^T={RHS(u_b)}
        F_n= λ < 0 ! The normal contact force is negative, contact occurs only if si gap<0
        F_f^*=ε_f·(u_b-u_b0)
        err_frctn=0
        IF(ABS(F_f^*) ≥ -f·F_n) THEN
            F_f= f·F_n·sign(u_b1) and the contact is in stick state
        ELSE
            F_f=F_f^* and the contact is in slip state
        END IF
        err_frctn=err_frctn+1 if the stick/slip state of the contact has changed
        iter_frctn=iter_frctn+1
    END LOOP ! end calculation of the friction forces
    CALCULATE « gap » functions
    λ= λ+ ε_ALM ·gap
END DO ! end calculation of the normal forces
```

Figure 7. Frictional contact algorithm using augmented Lagrange multipliers

The "contacts" loop

After converging the "outer" iterations loops for the normal forces, the state of the contacts must be checked. If the values of the Lagrange multipliers are positive, then the contact is open. This means that the initial assumption about the closed state of the contact is erroneous and the algorithm must be repeated by updating the state of the contact. A similar decision is taken if the contact is supposed open and the value of the gap function becomes negative. This is a third iterative loop that encompasses the "outer" one. Figure 8 displays the pseudo-code of the contact algorithm with friction. The algorithm contains three embedded loops. The first loop detects contacts, the second loop calculates the normal forces and the third loop the friction forces. The calculation of the nodal displacements given by the non-linear system (25) could be considered the fourth innermost loop.

The flow chart of the complete contact algorithm is depicted in Figure 17 of the Appendix 3. The decision algorithm describing the tests and the actions taken for updating the close/loose state of the contacts can be identified in the lower part of this flowchart.

```
! Initialize contacts
LOOP over bumps (i=1,Nbump)
    IF(gap_i<0) THEN cntct_i=1 ! the contact is closed
    ELSE cntct_i=0 ! the contact is loose
END LOOP over bumps
LOOP while contacts states are not converged
    LOOP while normal forces are not converged
        LOOP while friction forces are not converged
        END LOOP for friction forces
    END LOOP for normal forces
    ! Check contacts states
    cntct0=cntct ! save contacts states
    LOOP over bumps (i=1,Nbump) !
        IF(cntct0_i=1 .AND. lambda_i>=0) cntct_i=0 ! the contact changes from close to loose
        IF(cntct0_i=0 .AND. gap_i<0) cntct_i=1 ! the contact changes from loose to close
    END LOOP over bumps
    err_cntct=||cntct-cntct0|| !compute contact state error
END LOOP over contacts states
```

Figure 8. Algorithm for contact states detection and updating

Numerical results

The contact model is applied for the static analysis of the bump foil bearing structure described in [31]. It is a first generation foil bearing that was thoroughly analyzed in the literature and could now serve as a workbench. The characteristics of the foil structure are depicted in Figure 9 and listed in Table 1.

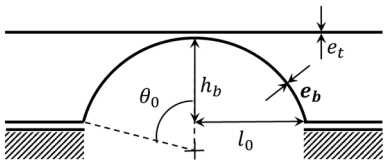

Figure 9. The geometry of the bump foil structure

Table 1 Geometric characteristics of the foil structure

Axial bearing length (mm), L	38.1
Shaft radius (mm), R	19.05
Radial clearance (μm), C_r	31.8
Number of bumps, N_{bump}	26
Foil thickness (mm), e_f	0.102
Young modulus (GPa), E	214
Poisson's ratio, υ	0.29
Bump pitch (mm), p	4.572
Bump length (mm), $2l_0$	3.556
Bump height (mm), h_b	0.508

The numerical tests consist of progressively pushing the rotor against the foil structure in positive and negative X and Y directions (Figure 1) by incrementing the eccentricity up to maximum radial displacement and then pulling the rotor back to the centered position. The force response of the compliant structure is calculated by summing the projected contributions of loaded bumps.

Foil structure free of manufacturing errors

The first comparisons are made with the model presented in [32] and for the bearing free of manufacturing errors. The results are depicted in Figure 10 for cases with friction (*f=0.1*) and without. Figure 10 depicts only the direct response forces (parallel to the rotor displacement), cross coupling forces being of small magnitude. The maximum radial displacement of the rotor was 79.5 µm (i.e. $2.5C_r$). This means the rotor interfered with the top foil over 47.7 µm.

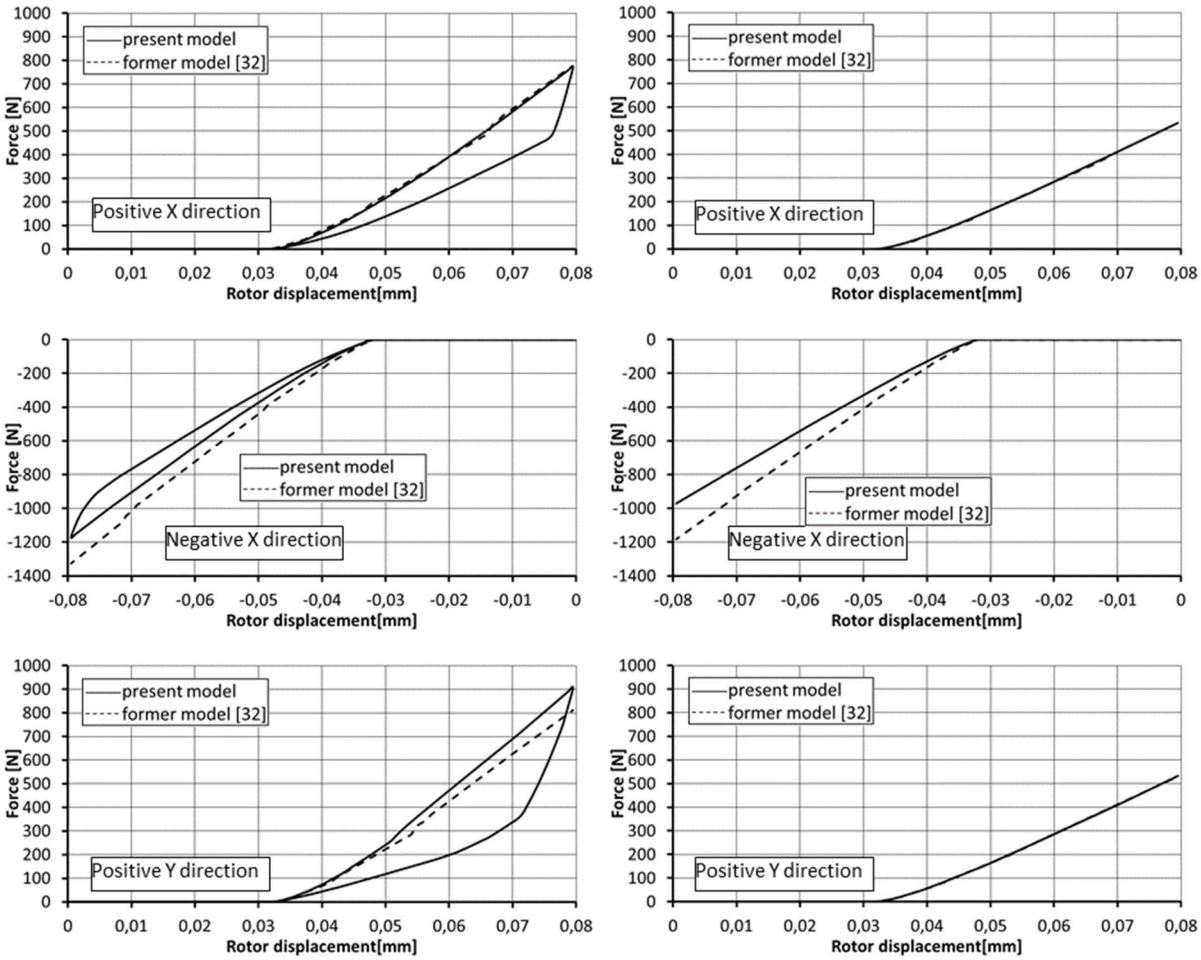

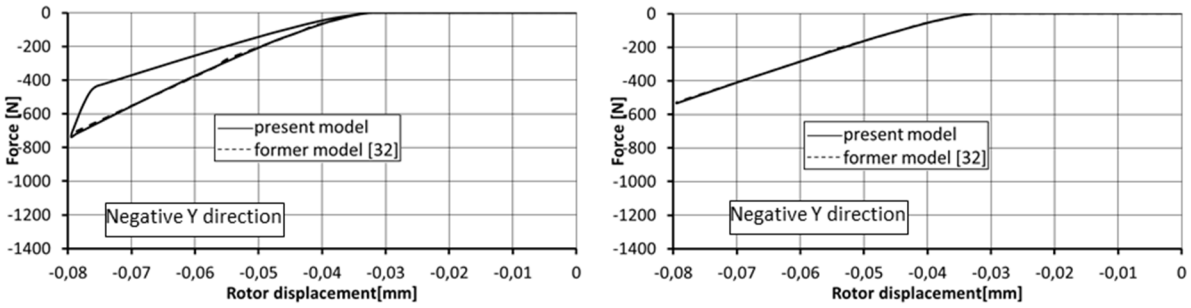

Figure 10. Direct structural response forces for rotor push and pull; comparisons between the new model and the model from [32] (left f=0.1, right f=0)

The former contact model from [32] considered Coulomb friction but was based on an algorithm that made no distinction between the static loading and unloading. Therefore, only a single (dotted) curve can be obtained. The present model makes a clear distinction between the loading and unloading part of the cycle with friction and therefore predicts the expected hysteresis loop. When friction is absent, both model predict a single loading-unloading curve.

The influence of friction on the static load is clearly shown by the results depicted in Figure 10. A friction coefficient of 0.1 leads to an increase of 20-60% of the static load depending on the loading direction.

Figure 10 shows that for the +X and –Y directions the results obtained with the contact model from [32] and the present model coincide while differences are present for the –X and +Y directions. These two latter loading cases correspond to radial displacements in the direction of the welding point of the foils (Figure 1). The differences can be explained when analyzing the load supported by each bump. Figure 11 depicts the load on each bump for the maximum radial displacement of the rotor (i.e. $2.5C_r$ or 79.5µm). It can be seen that for the -X direction, the first bump close to the welding is much more loaded than the rest of the bumps. While respecting this trend, the new model predicts a lower force for the first bump while the next bumps (from 2 to 5) are slightly more loaded. This result holds for both cases, with and without friction. This difference is due to the top foil that was absent in the former model and that enables a more uniform distribution of the bump load. The load predicted by the new model for the –X direction is therefore slightly lower.

For the +Y direction, the results in Figure 10 obtained with friction show a slightly larger force predicted by the new model while when friction is absent both models give the same results. Figure 11 shows that the forces predicted by the new model with friction are larger for bumps 2 to 4 (especially for bump 2) while being identical with the previous model for the rest of the bumps. This difference can be due to a combined effect of the top foil and the friction force. In all cases, the presence of the top foil in the new model extends the coupling between bumps while decreasing slightly the load gradient from bump to bump.

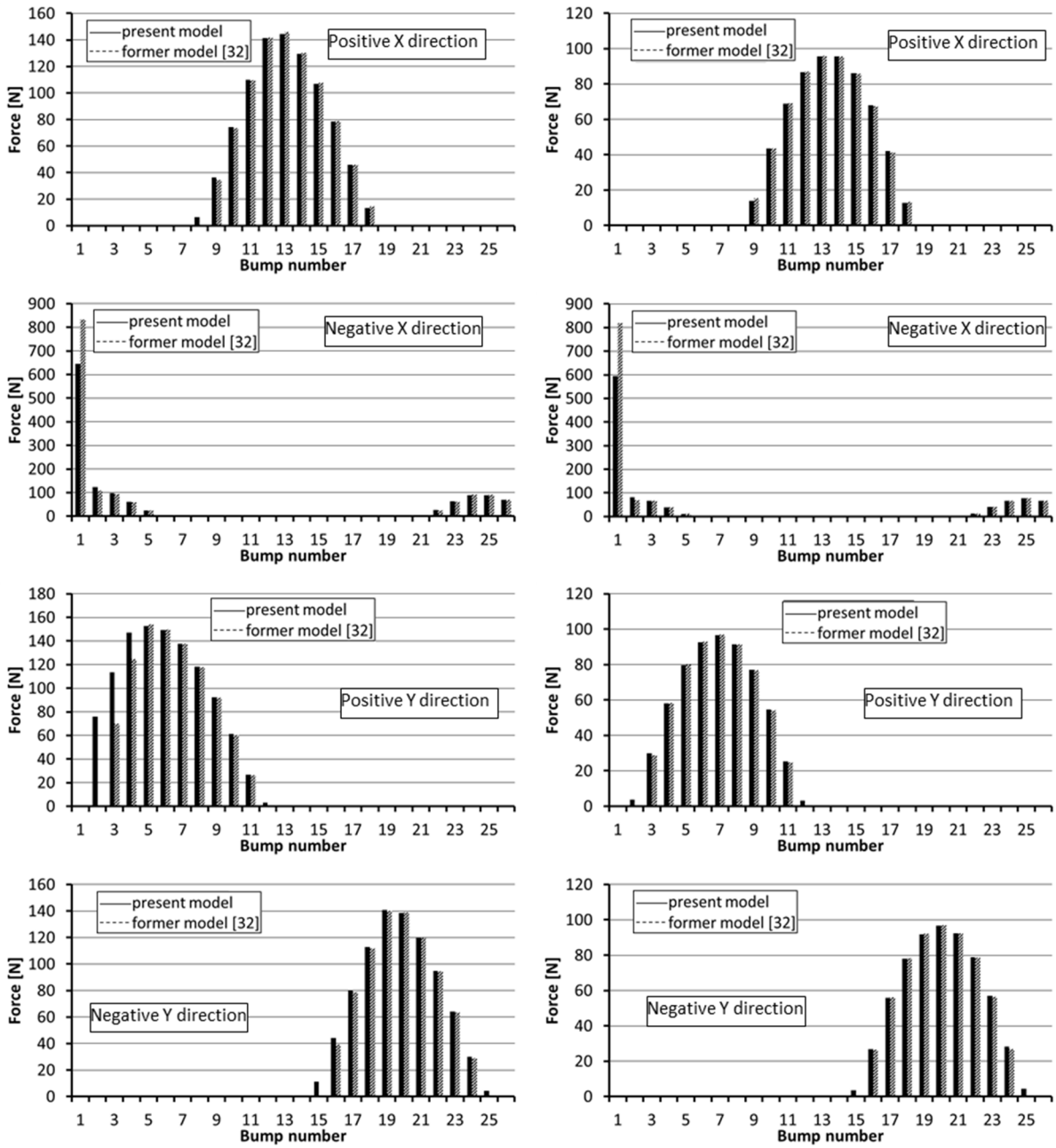

Figure 11. Bump loading for 2.5Cr radial displacement of the rotor; comparisons between the new model and the model from [32] (left f=0.1, right f=0)

Further comparisons made with a full non-linear elasticity model developed with a finite element commercial code are shown in Figure 12. Part of the results obtained with the finite element code were presented in [31]. In that reference, both the top and the bump foils were discretized with conventional shell elements and the sleeve was considered rigid. The interactions between the bumps, the sleeve and the top foil were taken into count with a penalty contact algorithm. Friction was considered by using the law of Coulomb.

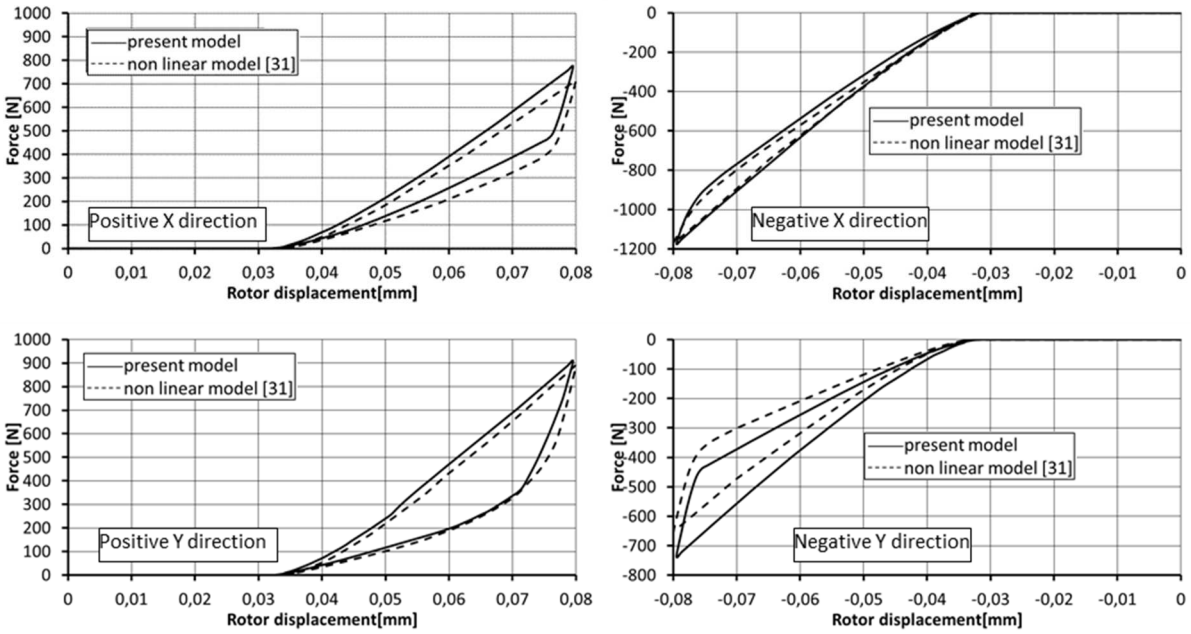

Figure 12. Direct structural response forces for rotor push and pull; comparisons between the new model and the non-linear results from [31] (f=0.1)

The results of the two models are very close but not identical. The differences come from the fact that in the non-linear structural model, the top foil and the bump foils are modeled as shells while the rotor and the sleeve were considered rigid. Surface contacts may then occur between discretization nodes and elements of the top and bump foils and are dealt with in a master-slave approach [41]. During loading and unloading, the master node may successively lay on the faces of different slave elements. Moreover, the contact is not reduced to a single pair of master-slave elements: many neighboring master nodes may lay on neighboring slave elements. This is a consequence of modeling the top foil and the bump foil as shells.

The model presented in this work for the bump foil is much simple. The bumps are replaced by trusses and the contacts between the elements of the foil structure may occur only in a node-to node approach: every node of a foil knows a priori the node of the other foil that it may contact. Even if a more elaborate model would have been used for the top foil the results would not have been different because the node to node contact is mainly imposed by the simplified bump foil model.

The present approach has the advantage of being very efficient in terms computation time compared to the complete structural model. For example, a loading-unloading cycle necessitates hours in the complete non-linear structural model and only minutes in the simplified model with 100 equally spaced intermediate steps.

Foil structure with manufacturing errors

Further comparisons between the new model and the full non-linear elasticity model from [31] can be made in the case of the foil bearing with manufacturing errors. Bump foil height manufacturing errors can be imposed in the new simplified model by using the gap functions.

It was considered that the manufacturing errors followed a normal distribution with an average value equal to the theoretical bump height (i.e. 508 µm) and a given standard deviation.

The results obtained for a rotor displacement of $2.5C_r$ toward +X are depicted in Figure 13 and Figure 14 for 10µm and 20µm standard deviations (i.e. 2% and 4% of the design bump height), respectively. The heights of the 26 bumps were randomly selected from a normal distribution. They are depicted as bars for each calculation case and are compared with the design bump height and the position of the rotor surface.

Six different cases are depicted in Figure 13 and Figure 14: the five cases presented in Figs. 12-13 of reference [31] plus an additional one. The prediction of the new simplified model coincide well with full non-linear elasticity model. For some cases, the radial forces predicted by the new simplified model are higher but the hysteresis loop delimited by the loading-unloading cycle is always well predicted.

The bump heights depicted as bars in Figure 13 and Figure 14 give also an insight of how the radial clearance is affected by manufacturing errors. The numerical analysis always needs a radial clearance for completely describing the geometry of the foil bearing. This design clearance can be even negative when it corresponds to an interference between the rotor and the top foil. However, due to the elasticity of the foil structure, the radial clearance is quite difficult to measure accurately even for an ideal foil structure, free of manufacturing errors. Therefore, the experimental measurements give a radial clearance affected by quite high uncertainties. For example, if the results in Figure 13 and Figure 14 would have been experimental data, the clearance in the +X direction could be estimated as the radial displacement of the rotor for which the direct structural force response F_x is lower than a given threshold. Figure 15 depicts the +X clearance estimated from Figure 13 and Figure 14 for 5N and 10N thresholds for F_x. The incertitude appears quite clear when comparing these results with the 31.8µm design value of the radial clearance (dotted line).

The difficulties encountered when measuring the radial clearance of real foil bearings (i.e. affected by manufacturing errors) can be explained by analyzing the deformation of the bumps and of the top foil during the loading and unloading process.

Figure 16 depicts the deformed top and bump foils for successive +X loading displacements. The left hand side and the mid column figures depict the unwrapped top and bump foils following the bearing circumference. For a better visualization of the contacts, the left hand column shows only the upper part of the bumps depicted as bars while the mid column depicts the entire bump height.

The right hand columns depict the same results in a cylindrical coordinate system. The successive snapshots in Figure 16a-e correspond to the points indicated in Figure 14. Figure 16a shows that interferences between the rotor, the top foil and the bump foil may be present even if the rotor is centered, although the bearing was designed with a 31.8µm radial clearance. This situation can occur even for lower standard deviation of the manufacturing errors. Figure 16b-e show how the top and bump foil are deformed by the displacement of the rotor. It can be observed that not only contacts between the bumps and the top foil change state (close/loose) but also contacts between the top foil and the rotor and between the bump foil and the casing may change state.

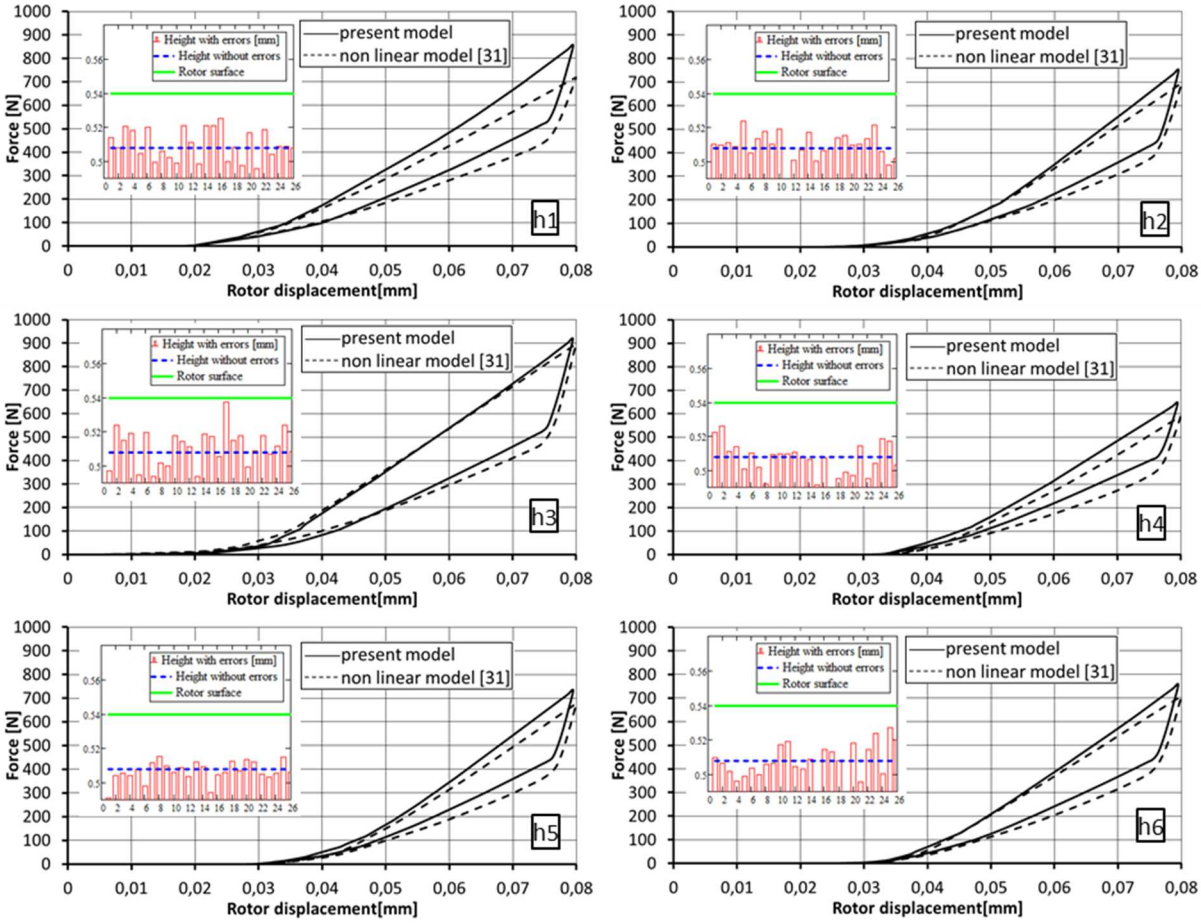

Figure 13. Direct structural response forces for rotor push and pull in "+X" direction; comparisons between the new model and the non-linear results from [31], bump heights manufacturing errors σ_{hb}=10µm

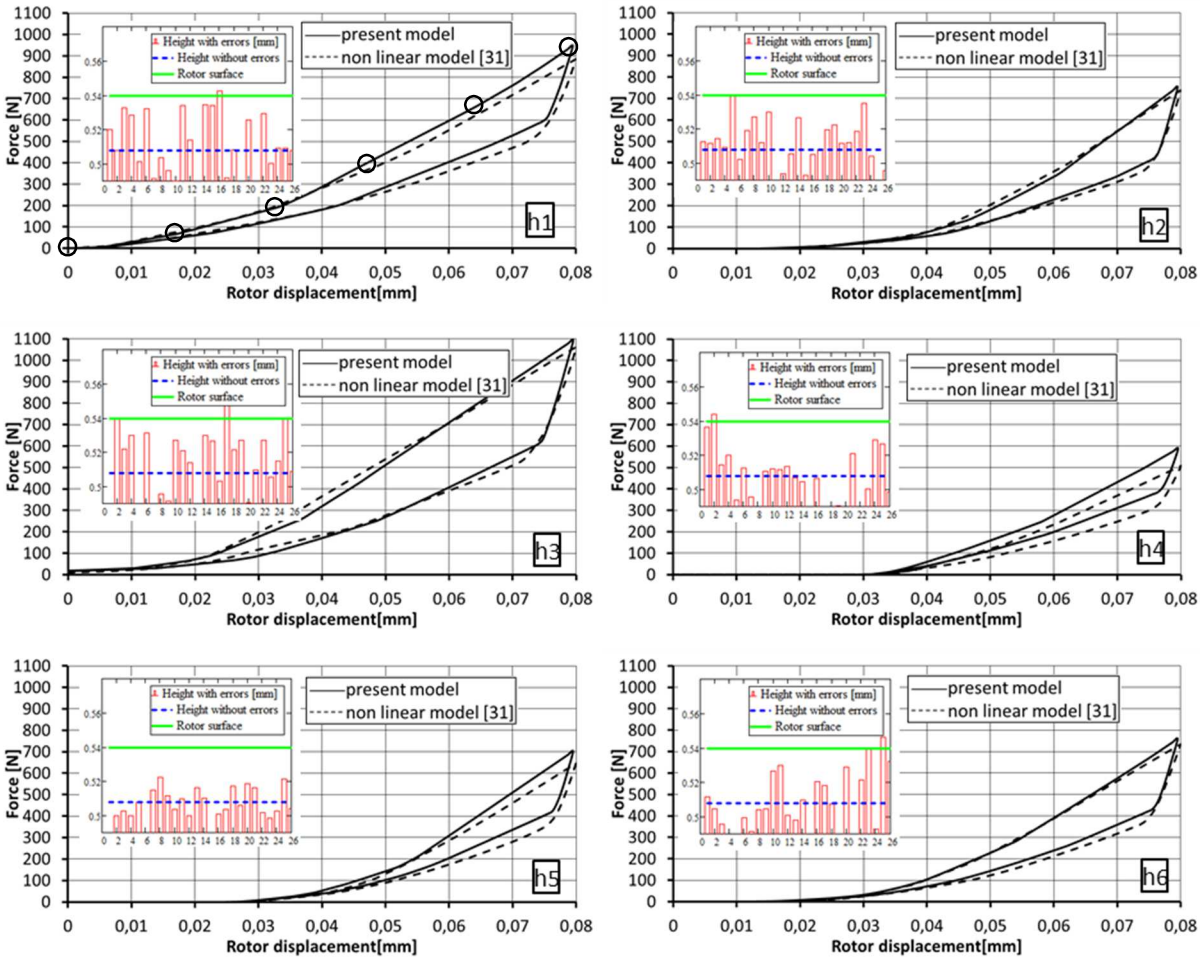

Figure 14. Direct structural response forces for rotor push and pull in "+X" direction; comparisons between the new model and the non-linear results from [31], bump heights manufacturing errors σ_{hb}=20µm

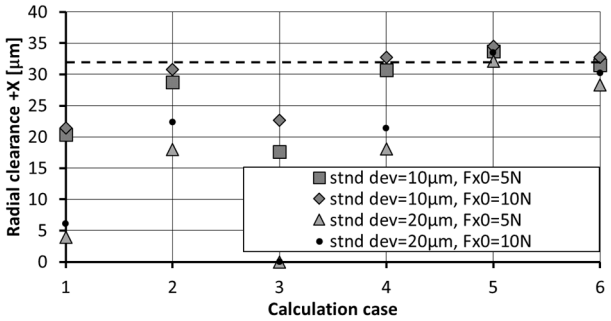

Figure 15. Radial clearance estimated from results depicted in Figure 13 and Figure 14

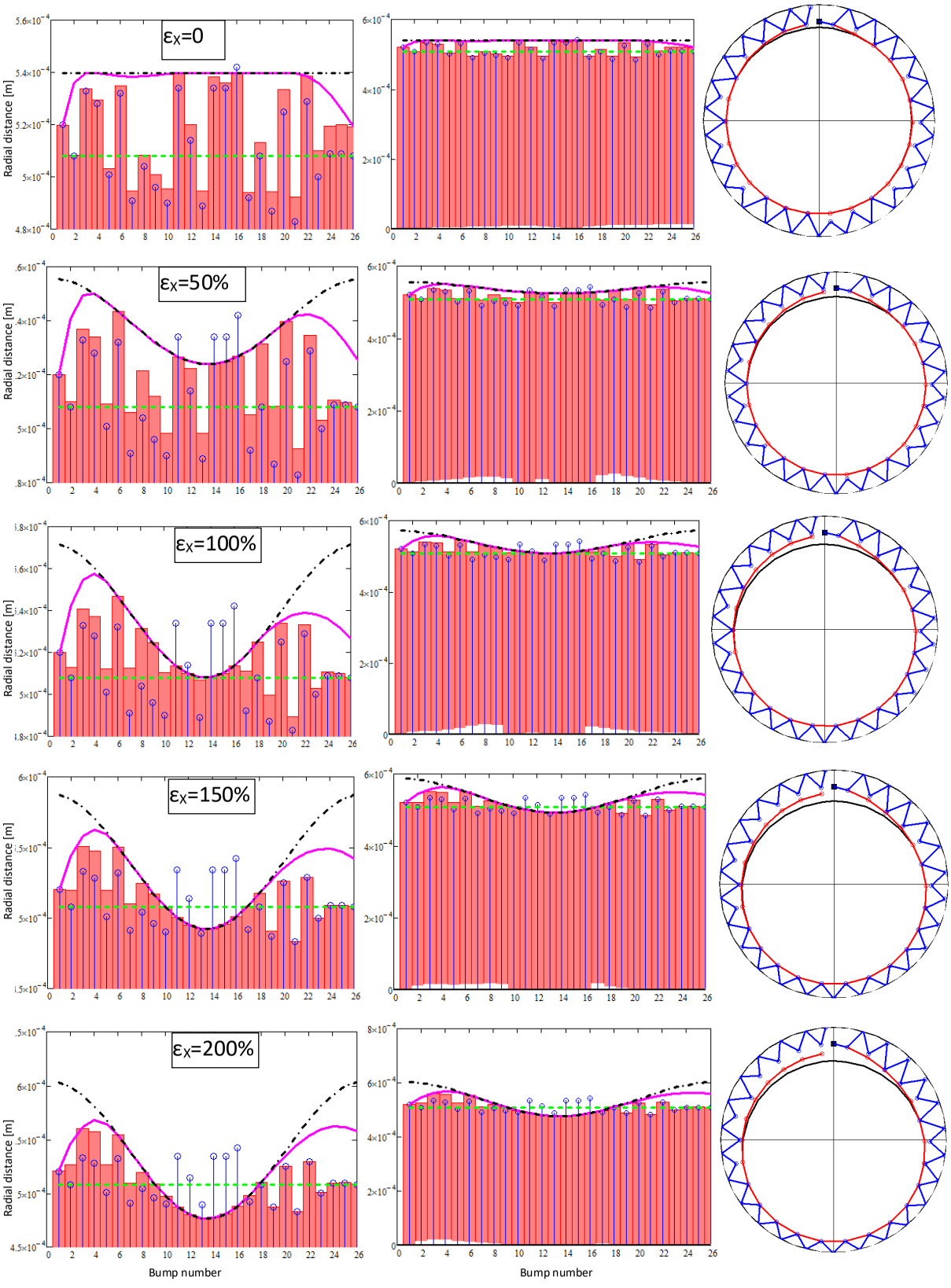
εX=0
εX=50%
εX=100%
εX=150%
εX=200%
Radial distance [m]
Bump number
Bump number

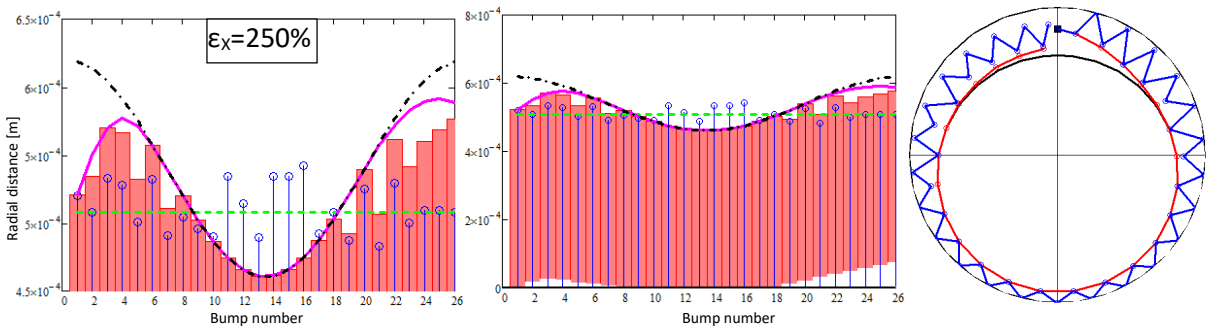

Figure 16. Top and bump foil deformation for successive +X rotor displacements (20 µm standard deviation of the bump height error). (left and center: unwrapped, right: Cartesian coordinate system)

Summary and conclusions

The present work introduces a new simplified model for taking into account the interactions with friction and gaps in a bump-type foil bearing structure. Simplified models are used for the bump and the top foil in order to reduce the computational effort. However, the contacts are dealt with in a very rigorous manner, by taking Coulomb friction into account and the possibility of having close/loose contacts. Three gap functions were employed for taking into account the close/loose states: between the bump foil and the sleeve, between the bump foil and the top foil and between the top foil and the rotor.

The algorithm was tested by simulating a static loading of the foil structure. The rotor was progressively pushed against the foil structure up to a maximum radial displacement and then pulled back to the centered position. The results of the present model were compared with simulations performed with a previous model that could not consider loose contacts and with a full non-linear elasticity code where the foils were modeled as shells. The results compared well and dissimilarities were explained by the different contact characteristics : the present simplified model deals with point contacts while the non-linear model handles contacts between surfaces.

The present model is able to deal very easily with manufacturing errors. This was proved by considering normally distributed errors of the bump height. It was shown that although the radial clearance of aerodynamic foil journal bearings is an important design parameter, its definition in a bearing with manufacturing errors is very difficult and prone to large measurement incertitude.

The contact algorithm proved to be very robust and efficient even when dealing with irregular gaps and friction forces.

Acknowledgement

The authors are grateful to Centre National d'Etudes Spatiales (CNES) and to Airbus Safran Launchers for supporting this work.

Nomenclature[5]

[5] Bold characters indicate vectors.

C_r, design radial clearance, [m]

E, Young modules of elasticity, [Pa]

e, foil thickness, [m]

F, force, [N]

f, friction coefficient

G, parameter in eq. (17)

g, gap, [m]

$\boldsymbol{J}$, jacobian matrix, [N/m]

$\boldsymbol{K}$, stiffness matrix, [N/m]

$k_1,\ldots,k_4$, stiffness of the truss model, [N/m]

L, bearing length, [m]

N_{bump}, number of bumps of the corrugated foil

N_{cntct}, number of closed contacts

N_{stick}, number of contacts in stick state

N_{slip}, number of contacts in slip state

N_{Rotor}, number of rotor/top foil contacts

R, bearing radius, [m]

r, distance between the rotor and the undeformed top foil, [m]

$\boldsymbol{S}$ or s_{ij}, elasticity matrix of the top foil, [m/N]

u, displacement, [m]

$\dot{u}$, sliding velocity, [m/s]

x, y, Cartesian coordinates

X, Y, axes of the Cartesian coordinates system

γ, parameter in eqs. (16) and (17)

ε, penalty parameter, [N/m]

ε_X, relative eccentricity in Figure 16

λ, Lagrange multiplier, [N]

θ, angular coordinate measured as in Figure 1

Π, potential energy, [j]

ν, Poisson coefficient

τ_f, time scale parameter, [s]

Subscripts

ALM, augmented Lagrange multiplier method

b, bump foil

f, friction

i, j, bump number

k, iteration number

LM, Lagrange multiplier method

n, normal

r, rotor

t, top foil

tg, tangential

P, penalty method

0, initial value

2b, corrugated foil with two bumps in Figure 3

Superscripts

$\bar{}$, variables kept constant during iterations

References

[1] Branagan, M., Griffin, D., Goyne, C., Untaroiu, A. Compliant Gas Foil Bearings and Analysis Tools. J. Eng. Gas Turbines Power 2016: 138(5): 054001.

[2] Heshmat, H., Walowit, J. A., Pinkus, O. Analysis of Gas-Lubricated Compliant Thrust Bearings. J. of Lubrication Tech 1983: 105(4): 638-646.

[3] Heshmat, H., Walowit, J. A., Pinkus, O. Analysis of Gas-Lubricated Foil Journal Bearings. J. of Lubrication Tech 1983: 105(4): 647-655.

[4] Iordanoff, I. Analysis of an Aerodynamic Compliant Foil Thrust Bearing: Method for a Rapid Design. J. Tribol 1999: 121(4): 816-822.

[5] Peng, J. P., Carpino, M. Calculation of Stiffness and Damping Coefficients for Elastically Supported Gas Foil Bearings. J. Tribol 1993: 115(1): 20-27.

[6] Rubio, D., San Andres, L. Structural Stiffness, Dry Friction Coefficient, and Equivalent Viscous Damping in a Bump-Type Foil Gas Bearing. J. Eng. Gas Turbines Power 2007: 129(2): 494-502.

[7] Kim, T.H., San Andres, L. Effect of Side Feed Pressurization on the Dynamic Performance of Gas Foil Bearings: A Model Anchored to Test Data. J. Eng. Gas Turbines Power. 2009: 131(1): 012501

[8] Ryu, K. Prediction of Axial and Circumferential Flow Conditions in a High Temperature Foil Bearing With Axial Cooling Flow. J. Eng. Gas Turbines Power. 2012: 134(9): 094503.

[9] Bou-Said, B., Grau, G., Iordanof, I. On Nonlinear Rotor Dynamic Effects of Aerodynamic Bearings With Simple Flexible Rotors. J. Eng. Gas Turbines. Power 2008: 130(1):012503.

[10] Bonello, P., Pham, H. M. The efficient computation of the nonlinear dynamic response of a foil-air bearing rotor system. J. Sound and Vibration. 2014: 333(15): 3459-3478.

[11] Carpino, M., Medvetz, L. A., Peng, J. P. Effects of Membrane Stresses in the Prediction of Foil Bearing Performance. Tribology Transactions. 1994: 37(1): 43-50.

[12] Peng, J. P., Carpino, M. Finite Element Approach to the Prediction of Foil Bearing Rotor Dynamic Coefficients. J. Tribol 1997: 119(1): 85-90.

[13] Carpino, M., Talmage, G. A Fully Coupled Finite Element Formulation for Elastically Supported Foil Journal Bearings. Tribology Transactions. 2003: 46(4): 560-565.

[14] Bruckner, R.J. Simulation and Modeling of the Hydrodynamic, Thermal and Structural Behavior of Foil Thrust Bearings. Doctoral Dissertation, Case Western Reserve University, Cleveland. 2004.

[15] San Andrés, L., Kim, T.H. Analysis of gas foil bearings integrating FE top foil models. Tribol. Int. 2009: 42(1): 111-120.

[16] Kim, D., Park, S. Hydrostatic Air Foil Bearings: Analytical and Experimental Investigations. Tribol. Int. 2009: 42(3): 413-425.

[17] Nielsen, B., Santos, I. F. Transient and steady state behavior of elasto-aerodynamic air foil bearings, considering bump foil compliance and top foil inertia and flexibility: A numerical investigation. Proc. IMechE. Part J: J. Eng. Tribol. 2017: 0(0): 1-19.

[18] Leister, T., Baum, C., Seemann, W. Computational Analysis of Foil Air Journal Bearings Using a Runtime-efficient Segmented Foil Model. J. Fluids Eng. 2018: 140(2): 021115.

[19] Roger Ku, C. P.,Heshmat, H. Compliant Foil Bearing Structural Stiffness Analysis-Part 1: Theoretical Model Including Strip and Variable Bump Foil Geometry. J. Tribol 1992: 114(2): 394-400.

[20] Lee, D.-H., Kim, Y.-C., Kim, K.W. The static performance analysis of foil journal bearings considering three-dimensional shape of the foil structure. J. Tribol 2008: 130(3): 031102.

[21] Lee, D.H., Kim, Y.C., Kim, K.W. The Dynamic Performance Analysis of Foil Journal Bearings Considering Coulomb Friction: Rotating Unbalance Response. Tribology Transactions 2009: 52(2): 146-156.

[22] Lee, D.H., Kim, Y.C., Kim, K.W. The Effect of Coulomb Friction on the Static Performance of Foil Journal Bearings. Tribol. Int. 2010: 43(5-6): 1065-1072.

[23] Lehn, A., Mahner, M., Schweizer, B. Elasto-gasdynamic modeling of air foil thrust bearings with a two-dimensional shell model for top and bump foil. Tribol Int. 2015: 100: 48-59.

[24] Li, C., Du, J., Yao, Y. Modeling of a multi-layer foil gas thrust bearing and its load carrying mechanism study. Tribol. Int. 2017: 114: 172-185.

[25] Barzem, L., Bou-Said, B., Rocchi, J., Grau, G. Aero-elastic bearing effects on rotor dynamics: a numerical analysis. Lubrication Science 2013: 25: 463-478.

[26] Kalker, JJ. Three Dimensional Elastic Bodies in Rolling Contact. Kluwer academics Publisher, London 1990: 314.

[27] Larsen, J.S., Varela, A.C., Santos, I.F. Numerical and experimental investigation of bump foil mechanical behavior. Tribol. Int. 2014: 74: 46-56.

[28] Zywica G. The static performance analysis of the foil bearing structure. Acta Mechanica et Automatica 2011: 5(4): 119-122.

[29] Temis, Y.M., Temis, M.Y., Meshcheryakov, A.B. Gas-dynamics Foil Bearing Model. J. Friction and Wear. 2011: 32(3): 212-220.

[30] Liu, J., Du, F. Simulation of Compliant Bump Foil Journal Bearing Using Coupled Reynolds Equation and Finite Element Model Method. Advanced Materials Research 2012: 479-481: 2499-2503.

[31] Fatu, A., Arghir, M. Numerical Analysis of the Impact of Manufacturing Errors on the Structural Stiffness of Foil Bearings, J. Eng. Gas Turbines Power 2018: 140(4): 041506.

[32] Le Lez, S., Arghir, M., Frêne, J. A New Bump-Type Foil Bearing Structure Analytical Model. J. Eng Gas Turbines Power 2007: 129(4): 1047-1057.

[33] Petrov, E.P., Ewins, D.J. Generic Friction Models for Time-Domain Vibration Analysis of Bladed Disks. J. of Turbomachinery 2004: 126(4): 184-192.

[34] Le Lez, S., Arghir, M., Frêne, J. Static and Dynamic Characterization of a Bump-Type Foil Bearing Structure. J. Tribol 2007: 129(1): 75-83.

[35] Le Lez, S., Arghir, M., Frêne, J. A Dynamic Model for Dissipative Structures Used in Bump-Type Foil Bearings. Tribol. Trans. 2009: 51(5): 562-572.

[36] Hryniewicz, P., Wodtke, M., Olszewski, A., Rzadkowski, R. Structural Properties of Foil Bearings : A Closed Form Solution Validated with Finite Element Analysis. Tribology Transactions 2009: 52(4): 435-446.

[37] Feng, K., Kaneko, S. Analytical Model of Bump-Type Foil Bearings Using a Link-Spring Structure and a Finite Element Shell Model. J. Tribol 2010: 132(2): 021706.

[38] Gad, A.M., Kaneko, S. A New Structural Stiffness Model for Bump-Type Foil Bearings: Application to Generation II Gas Lubricated Foil Thrust Bearing. J. Tribol; 2014: 136(4): 041701.

[39] Von Osmanski, S., Larsen, J.S., Santos, I.F. A fully coupled air foil bearing model considering friction – Theory & experiment. J. of Sound and Vibration 2017: 400: 660-679.

[40] Hoffmann, R., Munz, O., Pronobis, T., Barth, E., Liebich, R. A valid method of gas foil bearing parameter estimation: A model anchored on experimental data. J. Mechanical Engineering Science 2016: 0(0): 1-18.

[41] Wriggers, P, Zavarise, G. Computational Contact Mechanics. Springer-Verlag Brlin Heidelberg 2006: Second Edition: 518: 195-226.

[42] Zavarise, G., Wriggers, P., Nackenhorst, U. A Guide for Engineers to Computational Contact Mechanics. 2006. TCN Series on Simulation Based Engineering and Science. 176 pp.

Appendix 1

The stiffness matrix of the 4DOF/bump model depicted in Figure 4 can be cast as the sum of individual stiffness matrixes of each bump plus a coupling matrix.

$$\boldsymbol{K_{2b}} = \begin{bmatrix} 2k_1c^2 & 0 & -k_1c^2 & -k_1cs & 0 & 0 & 0 & 0 \\ 0 & 2k_1s^2 & -k_1sc & -k_1s^2 & 0 & 0 & 0 & 0 \\ -k_1c^2 & -k_1cs & k_2+k_1c^2 & k_1cs & 0 & 0 & 0 & 0 \\ -k_1sc & -k_1s^2 & k_1cs & k_1s^2 & 0 & 0 & 0 & 0 \\ 0 & 0 & 0 & 0 & 2k_1c^2 & 0 & -k_1c^2 & -k_1cs \\ 0 & 0 & 0 & 0 & 0 & 2k_1s^2 & -k_1sc & -k_1s^2 \\ 0 & 0 & 0 & 0 & -k_1c^2 & -k_1sc & k_2+k_1c^2 & k_1cs \\ 0 & 0 & 0 & 0 & -k_1sc & -k_1s^2 & k_1sc & k_1s^2 \end{bmatrix} + \begin{bmatrix} k_3+k_4 & 0 & 0 & 0 & -k_3 & 0 & 0 & 0 \\ 0 & 0 & 0 & 0 & 0 & 0 & 0 & 0 \\ 0 & 0 & k_2+k_1c^2 & -k_1cs & -k_1c^2 & k_1cs & -k_2 & 0 \\ 0 & 0 & -k_1cs & k_1s^2 & k_1sc & -k_1s^2 & 0 & 0 \\ -k_3 & 0 & -k_1c^2 & k_1cs & k_3 & 0 & 0 & 0 \\ 0 & 0 & k_1cs & -k_1s^2 & 0 & 0 & 0 & 0 \\ 0 & 0 & -k_2 & 0 & 0 & 0 & 0 & 0 \\ 0 & 0 & 0 & 0 & 0 & 0 & 0 & 0 \end{bmatrix} \quad \text{(A1)}$$

Equation (A1) suggests how the stiffness matrix of the corrugated foil with two bumps can be extended to an arbitrary number of bumps.

Appendix 2

For a robust solution of the non-linear system of equation (25), the discontinuous *sign* function must be approximated by a regular function. An approximation with the *atan* function is presently employed although other functions can be used (a.e. *tanh*)

$$sign\left(\dot{u}_{tg}^{(k)}\right) = \frac{2}{\pi} atan\left(\frac{u_{tg}^{(k)} - u_{tg}^{(0)}}{\tau_f}\right) \quad \text{(A2)}$$

The non-linear system for the displacements now yields:

$$\boldsymbol{F_{ALM}}(\boldsymbol{x}) = \boldsymbol{K_{ALM}} \begin{Bmatrix} u_{b,1} \\ u_{b,2} \\ u_{b,3} \\ u_{b,4} \\ u_t \end{Bmatrix} - \begin{Bmatrix} \varepsilon_f u_{b,1}^{(0)} ISTICK_t + f\bar{\lambda}_t \dfrac{2}{\pi} atan\left(\dfrac{u_{b,1} - u_{b,1}^{(0)}}{\tau_f}\right)(ISTICK_t - 1) \\ -\bar{\lambda}_t - \varepsilon_{ALM} g_{0_t} \\ \varepsilon_f u_{b,3}^{(0)} ISTICK_b + f\bar{\lambda}_b \dfrac{2}{\pi} atan\left(\dfrac{u_{b,3} - u_{b,3}^{(0)}}{\tau_f}\right)(ISTICK_b - 1) \\ \bar{\lambda}_b + \varepsilon_{ALM} g_{0_b} \\ \bar{\lambda}_t + \varepsilon_{ALM} g_{0_t} - \varepsilon_r r \end{Bmatrix} = 0 \tag{A3}$$

where $\boldsymbol{u} = \{u_{b,1} \quad u_{b,2} \quad u_{b,3} \quad u_{b,4} \quad u_t\}^T$.

Following the Newton-Raphson algorithm, the iterative solution writes:

$$\boldsymbol{u^{(k)}} = \boldsymbol{u^{(k-1)}} - \left[\boldsymbol{J_{ALM}^{(k-1)}}\right]^{-1} \boldsymbol{F_{ALM}^{(k-1)}} \tag{A4}$$

where the Jacobian matrix is:[6]

$$\boldsymbol{J_{ALM}} = \boldsymbol{K_{ALM}} - DIAG \begin{Bmatrix} \dfrac{2}{\pi} \dfrac{f\bar{\lambda}_t (ISTICK_t - 1)}{\tau_f \left\{1 + \left[\left(u_{b,1} - u_{b,1}^{(0)}\right)/\tau_f\right]^2\right\}} \\ 0 \\ \dfrac{2}{\pi} \dfrac{f\bar{\lambda}_b (ISTICK_b - 1)}{\tau_f \left\{1 + \left[\left(u_{b,3} - u_{b,3}^{(0)}\right)/\tau_f\right]^2\right\}} \\ 0 \\ 0 \end{Bmatrix} \tag{A5}$$

The inverse of this symmetric and positive definite matrix is quite rapid.

The time scale τ_f was calibrated with a trial and error approach. It should be underlined that the present numerical approximation of the Coulomb friction depends on two user calibrated parameters: ε_f and τ_f. They can be interpreted as the stiffness of the contacts between surface roughness and the time scale needed for changing the sign of the sliding velocity.

Appendix 3

A general flowchart of the complete contact algorithm is given in Figure 17.

[6] The *DIAG* function indicates a matrix with the first diagonal given by the argument vector.

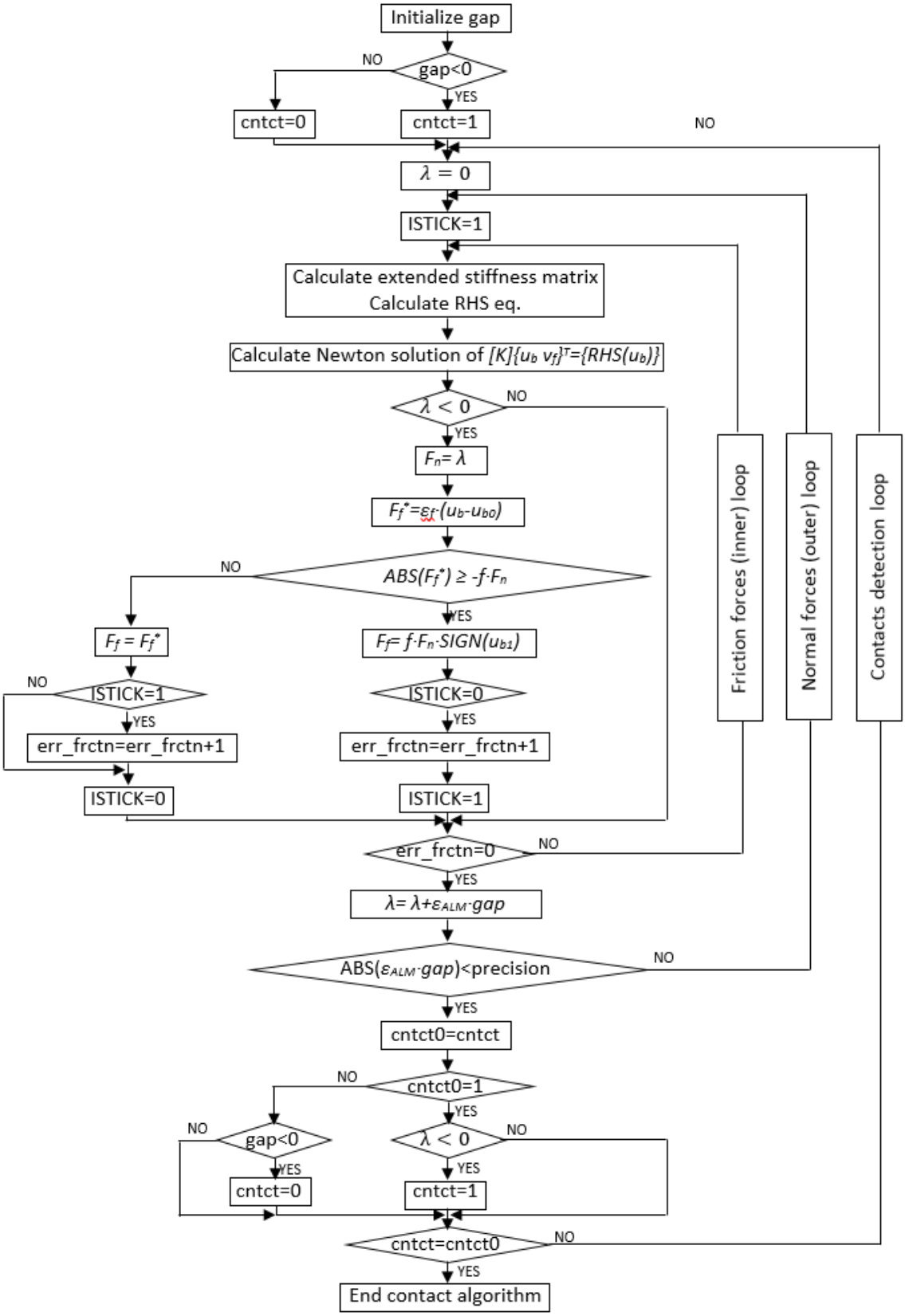

Figure 17. General flowchart of the contact algorithm for the foil bearing structure